Cell density couples tissue mechanics to control the elongation speed of the body axis

Changqing Lu[1,2,3,#], Joana M. N. Vidigueira[1,2,#], Christopher Chan Jin Jie[1,4,#], Alicja Maksymiuk[1], Fengzhu Xiong[1,2,*]

[1]Wellcome Trust / CRUK Gurdon Institute, University of Cambridge, Cambridge, UK
[2]Department of Physiology, Development and Neuroscience, University of Cambridge, Cambridge, UK
[3]Department of Anatomy, West China School of Basic Medical and Forensic Medicine, Sichuan University, Chengdu, China.
[4]Systems Biology programme, University of Cambridge, Cambridge, UK

[#]equal contribution
*correspondence: fx220@cam.ac.uk

SUMMARY

The vertebrate body forms by progressive addition and segmentation of tissues in an anterior to posterior direction. The posterior presomitic mesoderm (pPSM), which receives new cells from the tailbud, produces an expansive force that drives axis elongation[1–3]. Elongation moves an FGF gradient that controls the boundary placement of new segments in conjunction with the oscillatory genes of the segmentation clock[4]. As the period of the segmentation clock is insensitive to body size[5,6] or elongation progress[7,8], the number and size consistency of segments depend on stable, robust elongation. How elongation speed is constrained remains unknown. Here we utilised modeling and tissue force microscopy[9] on chicken embryos to show that cell density of the pPSM dynamically modulates elongation speed in a negative feedback loop. Elongation alters the cell density in the pPSM, which in turn controls progenitor cell influx through the mechanical coupling of body axis tissues. This enables responsive cell dynamics in over- and under-elongated axes that consequently self-adjust speed to achieve long-term robustness in axial length. Our simulations and experiments further suggest that cell density and activity under FGF signalling act synergistically to drive elongation. Our work supports a simple mechanism of morphogenetic speed control where the cell density relates negatively to progress, and positively to force generation.

During body axis elongation, the avian presomitic mesoderm (PSM) exhibits an anterior to posterior cell density gradient (from ~10.2k/mm^2 in the anterior PSM to ~6.5k/mm^2 in the pPSM[2]). The pPSM's particularly low cell density as compared to its surrounding tissues is associated with the high motility of cells and matrix production in this mesenchymal region, downstream of FGF signaling[1,3,10]. These processes cause the expansion of the pPSM which produces compressive stresses on the axial tissues and promotes their elongation[2,9]. Axial elongation in turn promotes the lateral movement of midline PSM progenitors into the pPSM (the progenitor cell influx), completing an engine-like positive feedback loop[2]. Cell density is therefore regulated by both pPSM expansion and progenitor influx, which work in opposite directions, making cell density a natural node for negative feedback in the system (Fig.1a).

In a recent 1-dimensional continuum model of elongation[11], progenitor influx was assumed to be proportional to the cell density gradient at the pPSM-tailbud/progenitor domain (PD) border, which effectively ties elongation (which reduces cell density) with proportional compensation of new cells, allowing the elongation speed to be stable. Whether this progenitor influx regulation takes place *in vivo* remains to be tested, while other body axis tissues such as the elongating notochord are also known to affect progenitor movement[2]. Here, to recapitulate 3D inter-tissue interactions, we developed agent (i.e., cell)-based models that follow the multi-tissue layout of the posterior body axis region. The simulation construct (~10k cells for the 3D PhysiCell model[12], comparable to the real tissue) contains a passive central axial tissue (representing the notochord and the neural tube) flanked by pPSM on both sides, and a PD on the posterior midline. This construct is further confined by rigid dorsal, ventral and lateral boundaries (representing ectoderm, endoderm and lateral plate mesoderm, respectively, modelled as non-cellular), and a posterior boundary that is modelled as either passive movable non-PSM cells or free space (Fig.1b).

In the 3D model containing only the tissue geometrical layout and motile pPSM cells, we found that a confined pPSM undergoing expansion is sufficient to drive most of the tissue flow features observed in embryos, including convergence and elongation of both the PSM and the axial tissue (Fig.1b). A 2D equivalent of the 3D model produces similar results and allows addition of new cells to the PD[2], therefore we used the much faster 2D model (~300-800 cells) to scale up the number of independent simulations. With progenitor influx, we reproduced stable elongation and a sustained cell density in the pPSM (Figs.1c-d). Reducing this influx led to a fall of cell density and slowing of the elongation progress. Using parameter sweeps, we also found that the cell activity of the pPSM (parameterized as cell-cell repulsion in the model) is the key factor for axis elongation under a constant initial cell density (Fig.1e). Thus, both the previous study[11] and our results show that the space created by elongation (driven by pPSM cell activity) needs to be continuously filled with new active cells to sustain axis elongation, although the underlying mechanisms of progenitor influx regulation employed by both models are distinct and not mutually exclusive. The former depends on the progenitor movement following the cell density gradient at the pPSM/PD border which could become steeper as a result of pPSM expansion[11]. The latter works through inter-tissue mechanics where the expanding pPSM compresses the axial tissue to elongate and consequently push the midline PSM progenitor cells in the PD to move laterally into the pPSM[2,9].

To alter cell density in the pPSM *in vivo* in a non-invasive manner, we extended the body axis of HH10-12 embryos by pulling and holding the tissue for 1-2 minutes from anterior to posterior (AP) at a contact point near the area pellucida edge (Fig.2a). Upon release of the stress, the bulk of the body axis exhibits an elastic recoil to restore the tissue length. However, the posterior end retains ~200μm of stable length increase, which is within the range of body axis length variation observed in unperturbed embryos at the same stages (Fig.S1a). The posterior extraembryonic tissues exhibit even more prominent plastic deformation with a smaller recoil. Elongation of the body axis stalls after pulling but the segmentation proceeds normally (Figs.S1b-c), suggesting that pulling affects elongation specifically. Using the Roslin Green Tg(CAGGs:eGFP)[13] embryos that provide high contrasts at tissue boundaries through the fluorescence signal, we found that the pulled embryos show a longer, darker PSM with unchanged width while the neighbouring neural

tube and notochord show a narrower tissue[9] (Fig.2b). This suggests that extension of the mesenchymal pPSM leads to a decrease in cell density, whereas extension of the epithelial axial structures causes tissue narrowing, mimicking their respective normal, active modes (expansion of the pPSM and convergent extension of the axial tissues, respectively) of elongation[2,3,14,15].

To validate the cell density change in the pPSM after pulling, we carefully compared stage- and location-matched control and pulled embryos using confocal imaging (Fig.2c). By counting labelled nuclei in confocal slices of the mPSM and pPSM regions along the body axis, we confirmed a marked decrease of cell density in the extended pPSM, particularly near the posterior end/progenitor domain (PD) of the tissue (~20% decrease, Fig.2d). We measured the medial-lateral cell density gradient across the PD-pPSM transition area using the fluorescence intensity and found that the gradient is steeper in pulled embryos (Fig.2e). Conversely, we compressed embryos using tissue force microscopy (TiFM)[9] for ~5 min before retrieving the probe. Analogous to pulled embryos, this operation generated an initial partial recoil leading to a stable shortening of ~100μm at the posterior end of the axis and a density increase in the pPSM (Figs.S1a, d-f). The posterior extraembryonic tissue was observed to creep anteriorly during compression and showed minimal recoil, consistent with its behaviour under pulling. These results show that tissues along the AP axis have a graded transition from stiffer and elastic to softer and plastic materials, corresponding to the reported gradients of extracellular matrix expression and cell organization[1,16]. In the compressed embryos, the cell density difference at the PD-pPSM boundary also becomes larger (Fig.2e).

To test how progenitor influx responds to cell density changes in the pPSM, we labelled the midline PSM progenitors in the PD by DiI injection and tracked their spread[2] (Fig.2f). Surprisingly, the progenitor spread is reduced after pulling (Fig.2g) against the steeper density gradient. This result shows that the feedback between elongation and cell influx does not occur at the PD-pPSM border as suggested previously[11]. Instead, our multi-tissue model suggests that the lower-density pPSM now produces a reduced stress (Fig.S2a) for the axial tissues, which in turn push less strongly on the PD (Fig.S2b), further reducing the progenitor influx into the pPSM (Fig.S2c). It is unlikely that the reduced stress is due to changed FGF activity in pPSM cells as their motility (measured through the spreading of labelled pPSM cell clusters) remains unchanged in extended embryos (Fig.2g). This motility is known to be controlled by the FGF activity level in the pPSM and inhibiting it causes stalled elongation[1]. Conversely, progenitor influx was observed to increase in the shortened embryos (Figs.2f-g), following the steeper density gradient and further increasing cell density in the pPSM which had already been increased directly by the compression (Fig.2e). These results together show that cell density variation in the pPSM is not only uncompensated by the progenitor influx, but also further exacerbated, likely through the mechanical coupling of the pPSM and the axial tissues.

To evaluate the consequences of the aggravated cell density change following pulling and compression, we simulated the effects of these perturbations by global (Fig.3a) and graded extension/compression from the posterior end (Figs.3b-d), and measured body axis elongation speeds over time. As expected from the significance of cell density in force generation, the compressed embryos with a higher density showed an immediate increase

of elongation speed while the pulled ones showed stalling of elongation. Interestingly, this response corrects for the length changes introduced by the mechanical perturbations, restoring axis length to that of the control, unperturbed embryos. Furthermore, this correction completes within a timeframe such that the average elongation speed, taking into account the introduced length changes, is indistinguishable from controls. The model thus suggests that cell density dynamics in the system stabilize the elongation speed against fluctuations, and constrain the axis length in longer term.

To test this hypothesis experimentally, we tracked the elongation of pulled and compressed embryos. Strikingly, the pulled embryos showed recovery of body axis length by slowing down elongation immediately after pulling (Figs.4a, c). The speed difference between controls and perturbed embryos corrects for the initial difference in length over time. Conversely, in compressed embryos, elongation speeds increase significantly in the first hour restoring the length to normal, despite the open wound in the posterior created by the insertion of TiFM probes (Figs.4b, d). These results show that body axis length and average elongation speed are robust properties of the system, possibly relying on the negative feedback through cell density and inter-tissue mechanics to react quickly to length deviations. As the acceleration and deceleration of elongation in response to cell density change should require the activity of pPSM cells under FGF signalling, we tested the elongation response to pulling while adding FGF protein to the posterior body. Unlike the control embryos that showed a transient boost of speed during 1-2 hours post treatment, the pulled embryos did not show a speed increase (Fig.4e), consistent with the idea that a certain cell density is required for active cells to generate the stresses for elongation. Conversely, the acceleration of compressed embryos was abolished in the presence of FGF signalling inhibitor PD1730741 (Fig.4f), indicating the shortened axis requires cell activities to produce the corrective response despite having a high density pPSM. These results show that FGF activity and cell density work cooperatively to regulate elongation speed during body axis formation, providing a driver and a constrainer, respectively (Fig.1a).

The mechanisms of morphogenetic speed control remain poorly understood. Our work reveals a simple general strategy for expanding mesenchymal tissues. Progress is driven - but also limited - by cell density, where the speed is constrained by the timescale that arises from the interactions between cell density regulators. This mechanism provides stability and long-term robustness that are also tunable by active factors (such as signalling). In the context of vertebrate body axis formation, this mechanism, in conjunction with the segmentation clock, ensures sequential somite formation at consistent sizes and appropriate number, with an invariant axis length for a reproducible body plan.

Acknowledgement: The authors thank C.U. Chan, O. Pourquie, N.J. Lawrence, S. Kato and members of the Xiong lab for reagents, technical assistance, and comments. This study is supported by a Wellcome Trust / Royal Society Sir Henry Dale Fellowship (215439/Z/19/Z) and an UKRI-EPSRC Frontier Research Grant (EP/X023761/1, originally selected as an ERC Starting Grant) to F.X. C.L. acknowledges a China Scholarship Council (CSC) scholarship (201906240004). A.M. acknowledges a Cambridge Centre for Physical Biology (CPB) summer scholarship.

Author Contributions: C.L., J.M.N.V., C.C.J.J. and F.X. designed the project. C.L. and J.M.N.V. performed the embryo experiments, A.M. and F.X. contributed to the embryo experiments. C.C.J.J., A.M. and F.X. performed the simulations. All authors analyzed the data and contributed to the manuscript. The authors declare no competing interest.

Methods

Chicken embryos. Wild type fertilized chicken eggs were supplied by MedEgg Inc. Transgenic eggs were supplied by the National Avian Research Facility (NARF) at University of Edinburgh. Eggs are stored in a 14°C fridge and incubated under 37.5°C ~45% humidity incubators (Brinsea). No animal protocol is required for the embryonic stages studied under the UK Animals (Scientific Procedures) Act 1986 (under 2 weeks, or 2/3 of gestation time for chicken). Embryos were staged following the Hamburger and Hamilton (HH) table[17] following extraction from the egg using the Early Chick (EC) culture protocol[18]. The embryos were maintained in a slide box with wet paper towels in incubators at all times except when snapshot images (<2min per embryo) were taken and when injection, pulling and compression experiments were performed either manually or on the TiFM system under room temperature. DiI injections were performed with a sharp-tipped glass needle with a Nanoject microinjector or mouth pipetting at 0.5mg/ml (2.5mg/ml DiI in ethanol diluted in Ringer's solution or PBS immediately prior to needle loading). The needle enters from the ventral side targeting the PD and the pPSM. The initial injected spots were allowed to diffuse for 2-4 hours to allow trackable single cells to appear around the spot, before pulling and compression perturbations were performed to the tissue. FGF signalling was inhibited by treating the embryos with 50 µl of a 4 µM solution of the FGF inhibitor PD1730741 (Bio-techne). To enhance FGF signalling, 50 µl solution of FGF8 recombinant mouse protein (424-FC-025/CF, R&D systems) at a concentration of 1 µg/ml was dropped by a pipette on the ventral surface of the embryo.

Manual and TiFM pulling and compression. HH10-12 embryos prepared on the EC culture plates were used. The embryos were under incubation prior to the experiments (conducted at room temperature) and returned to incubator after the recoil stopped (~2min, embryos left in room temperature for extended times do not show further recoil or elongation). Pulling experiments were performed both manually as well as on the TiFM. Compression experiments were performed on the TiFM alone. For manual pulling, a tungsten rod (~50µm diameter) was installed on a surgical needle holder (Fine Science Tools) and brought to contact with the embryo at the boundary between Area Opaca and Area Pellucida at the axial midline point. Gently, without creating tearing damage, the tissue was pulled posteriorly with visible strain of the body axis. A ~30% strain from head to tail was achieved gradually and maintained for 1-2 minutes before retracting the rod. The tissue showed a recoil that stopped after 1 minute, retaining ~100-200µm of posterior elongation (~4% strain). For TiFM pulling, a cantilever probe was inserted into the posterior cells to perform the loading, mimicking the manual protocol to increase consistency. For compression experiments, as individual tissues tend to decouple when the compressed interface between the probe and the tissues is small, a tailored piece of aluminium foil that covers both pPSM cross-sections and the axial tissues was used. The foil was inserted just posterior to the PSM progenitor domain (PD). The axis was held for 5-6 minutes after ~600µm of posterior to anterior foil movement and then the foil was directly retracted from the embryo. A thin slit wound was left in the posterior cells which

normally healed later. The recoils of the tissue were recorded in timelapse movies and the movement was fit with a stress relaxation model to confirm the presence of a long-term plastic length change (only embryos that showed at least 50µm (~1.5% strain) of shortening were further analyzed). The embryos were then returned to the incubator and imaged regularly to measure axis elongation and cell spreading if labelled.

Imaging. Snapshots of the embryos were taken with a stereomicroscope (MZ10F, Leica). Confocal images were taken with a laser scanning microscope with a 40X objective (on a Leica SP5 or a Nikon Sora). For live imaging on the TiFM, cultured embryos were transferred to a 35mm glass bottom dish (VWR) with a thin layer of albumen (200µl) and imaged using a Zeiss Axio Observer 7 microscope base as part of the TiFM system with a 5x or 10x objective at room temperature.

Modeling. PhysiCell is an open-source, agent-based 3D cell simulator for mechanistic modeling of multicellular systems previously described[12]. In this work the mechanics module of the simulator was used to implement four main mechanical interaction parameters: cell-cell adhesion, cell-cell repulsion, cell-boundary adhesion and cell-boundary repulsion. The model (Supplemental Software 1, available at https://github.com/xionglab/project_elongation) resolves the net force resulted from these interactions and updates cell movement per iteration. The mechanical equation shown below relates the cell's current velocity v_i as a function of these terms and a movement term $v_{i,mot}$, which describes active cell motility. Cell positions are x_i. $\phi_{n,R(x)}$ is an adhesion interaction potential, $\psi_{n,R(x)}$ is a repulsion interaction potential function. C^i_{cca} and c^i_{ccr} are the ith cell's cell-cell adhesion and repulsion parameters, R_i is its radius, and $R_{i,A}$ is its maximum adhesion distance. $D(x)$ is the cell's distance to the nearest boundary and $n(x)$ is a unit vector normal to the boundary.

$$v_i = \sum_{j \in N(i)} \Big(\overbrace{-\sqrt{c^i_{cca} c^j_{cca}} \nabla \phi_{1,R_{iA}+R_{jA}}(x_i - x_j)}^{\text{cell-cell adhesion}} - \overbrace{\sqrt{c^i_{ccr} c^j_{ccr}} \nabla \psi_{1,R_i+R_j}(x_i - x_j)}^{\text{cell-cell repulsion}} \Big).$$

$$\underbrace{-c^i_{cba} \nabla \phi_{1,R_{iA}}(-d(x_i) n(x_j))}_{\text{cell-boundary adhesion}} - \underbrace{c^i_{cbr} \nabla \psi_{1,R_i}(-d(x_i) n(x_j))}_{\text{cell-boundary repulsion}} + v_{i,mot}$$

Simulations were run for a total of 7200 virtual minutes on a field of ~10k cells, using the following parameters:

Cell type	Motility (directionless)	Relative Adhesion	Relative Repulsion	Adhesion Distance
Axial	0	0.1	0.1	2.5
Presomitic Mesoderm	5	0.05	2	2.5
Posterior Cells	0	2	0.5	2.5

For simplicity, axial cells including the notochord and neural tube were considered as one passive tissue (the motility of these cells was 0) that only deforms by the forces from the flanking PSM. The posterior cells were also simulated as non-migratory and passive which

were displaced by an intermediate repulsion from the axial cells and the PSM cells. It is worth noting that these assumptions ignore the active intercalations of the axial cells as the tissues elongate[2] and also the medial to lateral movements of the posterior cells. The output of the 3D model was compared with a simpler 2D model previously described[2]. No significant qualitative differences of tissue and cell behaviors were observed.

The 2D model was then used to perform computationally demanding parameter explorations to understand how the various mechanical parameters affect axis elongation and convergence. To assist the parameter space coverage, an unbiased, unsupervised shallow neural network (created using Matlab, Mathworks) that did not require prior knowledge about the output targets was utilized to handle a total of 9193 outputs from the simplified 2D model. The 5 variables, PSM-PSM repulsion, NC-NC repulsion, Posterior-Posterior repulsion, PSM-NC repulsion and PSM-Posterior repulsion were used as inputs (table below), and the length and width of the axial tissue (represented by NC cells) were used as targets for the model. Both inputs and outputs were scaled before being used for training. 70% of the samples were used as training data, 15% as validation, and 15% as testing. The raw simulation data and the trained network and associated protocols are provided in Supplementary Software 1.

Value	PSM-PSM Repulsion	NC-NC Repulsion	Posterior-Posterior Repulsion	PSM-NC Repulsion	PSM-Posterior Repulsion
Minimum	5	1	0.1	20	10
Maximum	45	16	1.1	80	60

To model progenitor influx and axis length changes, we used a modified version of the previously described 2D model[2] in Matlab (Mathworks) (see Supplementary Software 2). To simulate pulling and compression, the cell positions were adjusted as compared to control in either global deformation or a data-matched decaying deformation from posterior to anterior. In the former, the whole simulated field of cells was compacted or stretched equally along the AP axis. In the latter, stretching and compression were implemented in an exponential manner. The posterior cells were displaced more which was consistent with the experimental data probably because the tissues closer to the pulling rod or compressing foil were less elastic. The posterior 75% of the cells in the simulation field were pulled or compressed to reach a ±10%-15% total strain, to be consistent with the experimental data. Body axis elongation (measured by the average position of the 4 posterior-most axial cells) was then followed in the simulation for 6000 iterations per independent simulation. Groups of 10-40 simulations per control or test group were performed.

Data analysis. Images and movies are processed by ImageJ (NIH) and Powerpoint (Microsoft). Scale bars are first set with control images with objects of known sizes. To measure cell density, high resolution confocal Z-stacks of DAPI staining were used for manual nuclei count in ImageJ. For transgenic fluorescent embryos, the fluorescent signal from the PSM and PD tissue was used as an approximate measure of cell density, which was validated by DAPI counts. To measure cell spreading, DiI-injected tissue areas in the pPSM and the PD were marked as ROIs at different points with trackable cells forming the edges. The areas of these ROIs were then compared to yield a percentage change over

time. To measure the elongation speed, the distance between a fixed somite pair (somites 2-5) and the posterior end of the body axis was taken. DiI was injected to mark the posterior end to minimize measurement inaccuracies due to tissue deformation after pulling. Results were plotted with statistical tests performed using Excel (Microsoft) and custom R code.

References

1. Bénazéraf, B. *et al.* A random cell motility gradient downstream of FGF controls elongation of an amniote embryo. *Nature* **466**, 248–252 (2010).

2. Xiong, F., Ma, W., Bénazéraf, B., Mahadevan, L. & Pourquié, O. Mechanical Coupling Coordinates the Co-elongation of Axial and Paraxial Tissues in Avian Embryos. *Dev Cell* **55**, 354-366.e5 (2020).

3. Michaut, A. *et al.* Activity-driven extracellular volume expansion drives vertebrate axis elongation. *bioRxiv* 2022.06.27.497799 (2022) doi:10.1101/2022.06.27.497799.

4. Dubrulle, J., McGrew, M. J. & Pourquié, O. FGF Signaling Controls Somite Boundary Position and Regulates Segmentation Clock Control of Spatiotemporal Hox Gene Activation. *Cell* **106**, 219–232 (2001).

5. Cooke, J. Scale of body pattern adjusts to available cell number in amphibian embryos. *Nature 1981 290:5809* **290**, 775–778 (1981).

6. Ishimatsu, K. *et al.* Size-reduced embryos reveal a gradient scaling-based mechanism for zebrafish somite formation. *Development (Cambridge)* **145**, (2018).

7. Oginuma, M. *et al.* A Gradient of Glycolytic Activity Coordinates FGF and Wnt Signaling during Elongation of the Body Axis in Amniote Embryos. *Dev Cell* **40**, 342-353.e10 (2017).

8. Denans, N., Iimura, T. & Pourquié, O. Hox genes control vertebrate body elongation by collinear Wnt repression. *Elife* **2015**, (2015).

9. Chan, C. U. *et al.* Direct force measurement and loading on developing tissues in intact avian embryos. *Development (Cambridge)* **150**, (2023).

10. Delfini, M. C., Dubrulle, J., Malapert, P., Chal, J. & Pourquié, O. Control of the segmentation process by graded MAPK/ERK activation in the chick embryo. *Proc Natl Acad Sci U S A* **102**, 11343–11348 (2005).

11. Regev, I., Guevorkian, K., Gupta, A., Pourquié, O. & Mahadevan, L. Rectified random cell motility as a mechanism for embryo elongation. *Development (Cambridge)* **149**, (2022).

12. Ghaffarizadeh, A., Heiland, R., Friedman, S. H., Mumenthaler, S. M. & Macklin, P. PhysiCell: An open source physics-based cell simulator for 3-D multicellular systems. *PLoS Comput Biol* **14**, e1005991 (2018).

13. McGrew, M. J. *et al.* Localised axial progenitor cell populations in the avian tail bud are not committed to a posterior Hox identity. *Development* **135**, 2289–2299 (2008).

14. Mongera, A., Michaut, A., Guillot, C., Xiong, F. & Pourquié, O. Mechanics of anteroposterior axis formation in vertebrates. *Annu Rev Cell Dev Biol* **35**, 259–283 (2019).

15. Kunz, D. *et al.* Downregulation of extraembryonic tension controls body axis formation in avian embryos. *Nature Communications 2023 14:1* **14**, 1–15 (2023).

16. Mongera, A. *et al.* A fluid-to-solid jamming transition underlies vertebrate body axis elongation. *Nature* **561**, 401–405 (2018).

17. Hamburger, V. & Hamilton, H. L. A series of normal stages in the development of the chick embryo. *J Morphol* **88**, 49–92 (1951).

18. Chapman, S. C., Collignon, J., Schoenwolf, G. C. & Lumsden, A. Improved method for chick whole-embryo culture using a filter paper carrier. *Developmental Dynamics* **220**, 284–289 (2001).

Figures

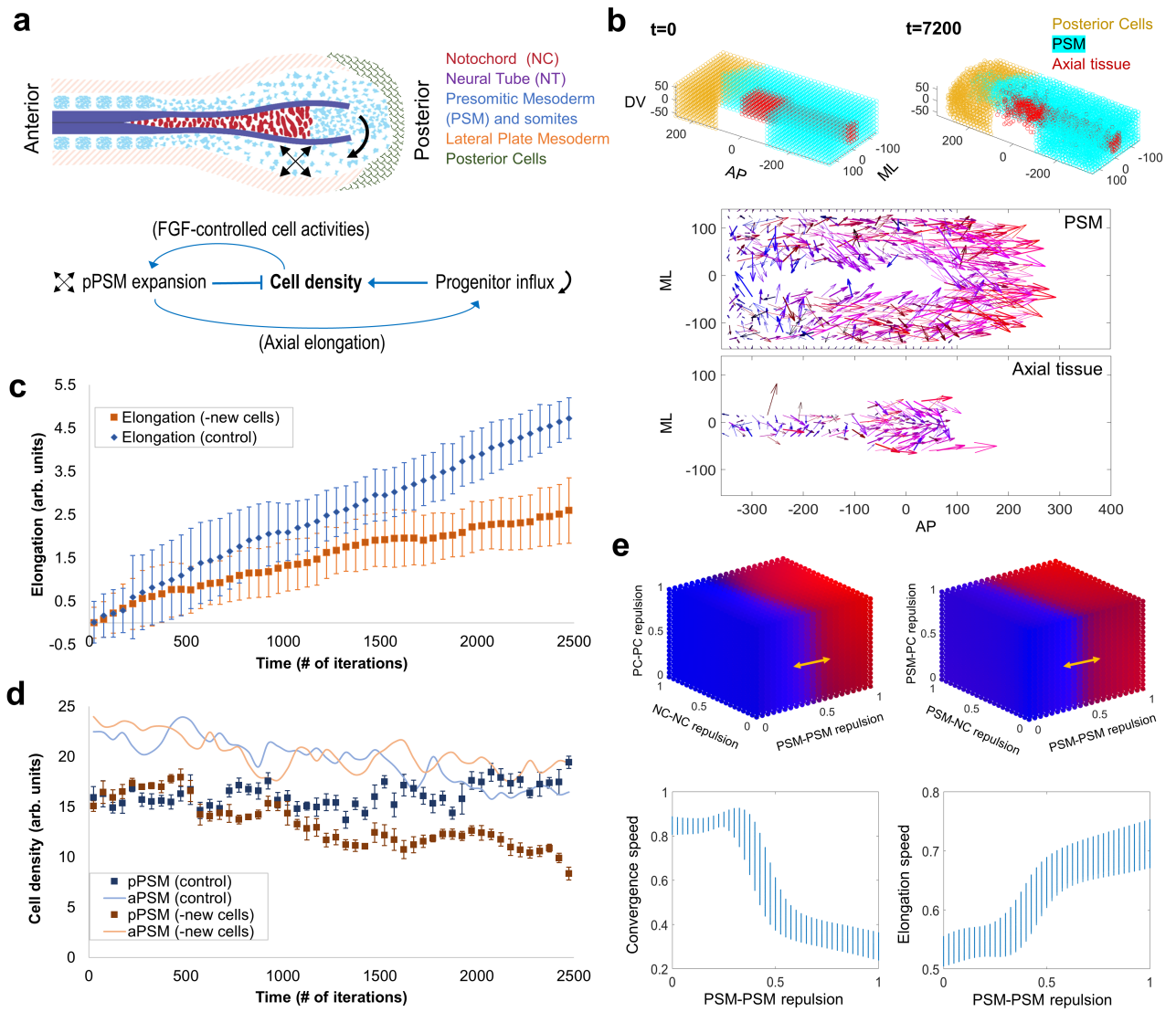

Figure 1. Modeling axis elongation and pPSM cell density dynamics. a. Schematic of the tissue organization of the posterior body axis. The network diagram depicts the interactions that alter cell density in the pPSM. **b.** Visualization of PhysiCell 3D tissue layout, t (time) indicates the simulation minutes. A portion of the PSM (blue) has been made invisible, allowing for the shape of the underlying axial tissue (red) to be seen. DV, dorsal-ventral axis, dorsal to the top; AP, antero-posterior axis, posterior to the top left; ML, medio-lateral axis, axial tissue is the medial. Bottom plots show the vectors of cell displacements in a representative simulation. Arrow length represents the displacement of cells (magnitude) and direction (also color-coded, blue represents convergence behaviours, red represents elongation behaviours, thickness indicates displacements in Z, i.e., DV). Both the axial tissues and pPSM are observed to converge along the ML axis and elongate along the AP axis towards the posterior. The anterior regions of the tissues are dominated by convergence (lateral to medial) movements (mostly blue arrows). The posterior region is dominated by elongation (anterior to posterior, mostly red arrows) and

convergence extension (mostly purple arrows). **c.** Simulation of elongation in the 2D model without new cell addition from the progenitor domain. The total progress of elongation was measured over simulation time. 20 simulations were performed in each condition and 50 adjacent time points were binned to generate the plot. Error bars are ±SD of the binned mean. **d.** Cell density in the simulated PSM corresponding to panel **c**. Cells were counted in grids specified (anterior and posterior PSMs are labelled as aPSM and pPSM, respectively) in the simulated PSM as a function of distance to the axis end. A decrease in cell density in the pPSM of the simulations lacking new cell addition is observed. The density rise of the pPSM towards the end was a simulation artefact as the axial cells which do not divide in the model run out, causing pPSM cells to accumulate on the midline. **e.** Parameter space sweep of cell-cell interactions using a simplified 2D model (without new cell addition). Each cube compares 2 independent scaled parameters with PSM-PSM repulsion on their effect on tissue movement (blue, convergence dominated; red, elongation dominated), accounting for all 5 parameters used in the model. Bottom plots show the impact of PSM-PSM repulsion in comparison to NC-NC and PC-PC repulsions (shown as the vertical range of the blue bars). PSM-PSM repulsion appears to be the determinant factor of the behaviour of the system, with a sharp transition boundary from convergence dominated to extension/elongation dominated cell movements around 0.5. PC, posterior cells; NC, notochord cells, here representing the axial tissues.

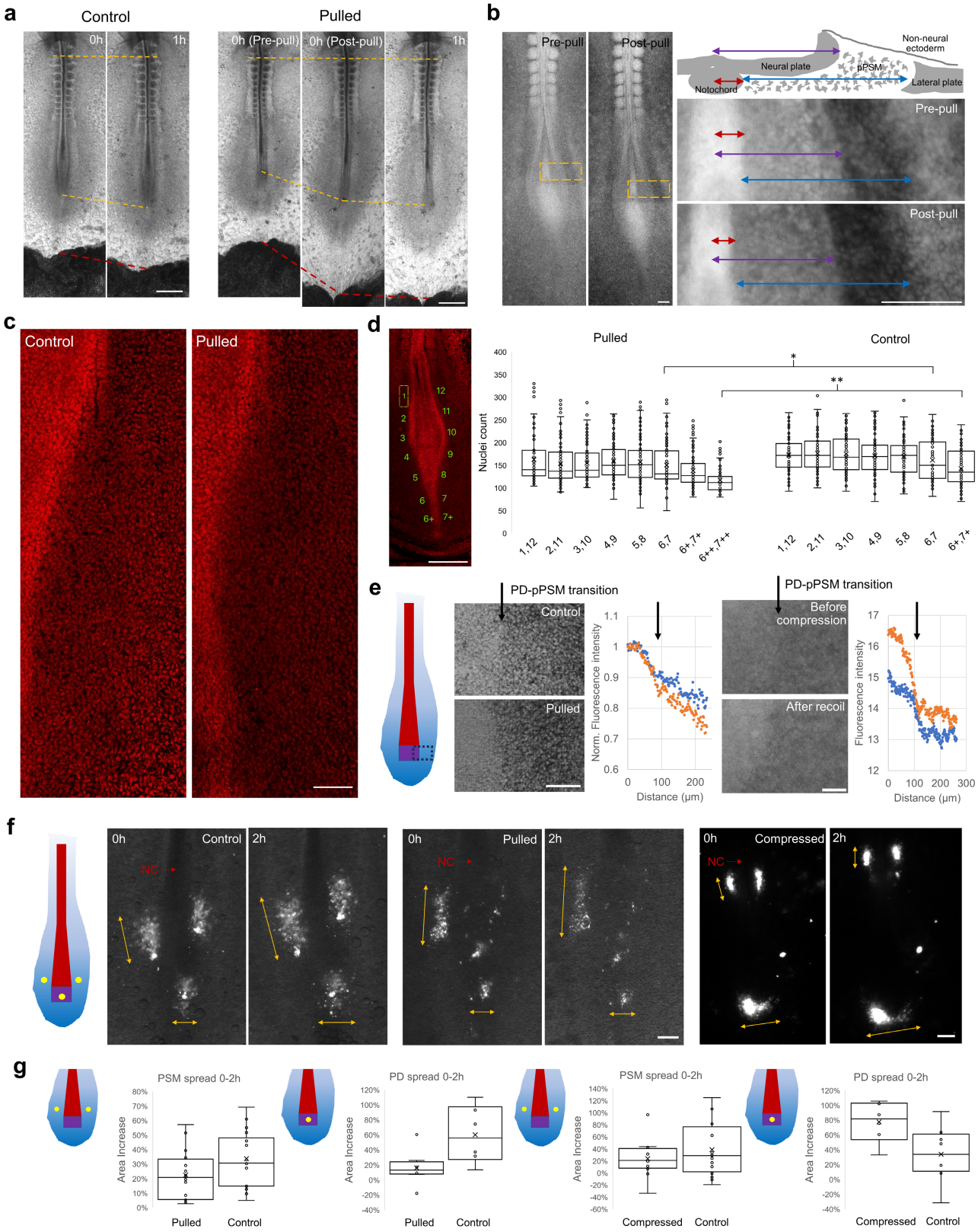

Figure 2. PSM cell density changes in extended and shortened embryos. a. Deformation of the body axis and surrounding tissues after pulling. Ventral views with

anterior to the top (same in other panels). The ends of the top yellow dashed lines mark a somite reference and the ends of the middle yellow dashed lines mark the end of the axis. The bottom red dashed lines mark the boundary of area pellucida (light grey) and area opaca (dark grey). Scale bars: 500μm. **b.** GFP+ embryo pulled by a TiFM probe. Images show the GFP signal. Orange boxes on the embryo images (left) mark the regions of zoomed-in views (right). The schematic shows the cross-sectional arrangement of body axis tissues (right side). Red, purple and blue double arrows indicate the width of the notochord, neural plate and pPSM, respectively. Scale bars: 100μm. **c.** Confocal images of the pPSM area on the right side of the axis. DAPI signal is shown in red. The denser regions to the left are the axial tissues and PD. Scale bar: 100μm. **d.** Cell counts of the areas marked in the image. Counting was done manually on 20 confocal slices through the PSM tissue per embryo (n=6 pulled embryos and n=4 control embryos) in equal areas of 100x200μm as shown with the numbered yellow box in the image. Additional pairs of posterior end areas (6+, 7+, 6++,7++) were counted to match the extended length in the pulled embryos with regions in control embryos. *p=0.037, **p=3e-7, 2 tailed t-tests. Scale bar: 500μm. **e.** Density difference assessed by fluorescence intensity in GFP+ embryos at the PD-pPSM transition. The illustration shows the area imaged (dotted black box. red, notochord; purple, PD; graded blue, PSM, same for the following panels). Arrows mark the transition boundary on images and the plots. The pulling confocal images (maximum projection) use 2 different embryos, the fluorescent intensity was normalized to the PD before comparison. The compression images were taken with epifluorescence in the same embryo (2 min post probe retraction). Scale bars: 100μm. **f.** Tracking cell clusters by injected DiI in pPSM and PD (yellow spots in the illustration). Double arrows show the spread of the clusters. NC, notochord. Scale bars: 100μm. **g.** Cluster area (segmented around the edge for pulling experiments and calculated as a product of AP and LM spreads for compression experiments, respectively, due to different image qualities) changes over time. PSM spread pulled n=16, control n=18, p=0.076. PD spread pulled n=8, control n=6, p=0.019. PSM spread compressed n=12, control n=16, p=0.338. PD spread compressed n=6, control n=8, p=0.036. 2 tailed t-tests.

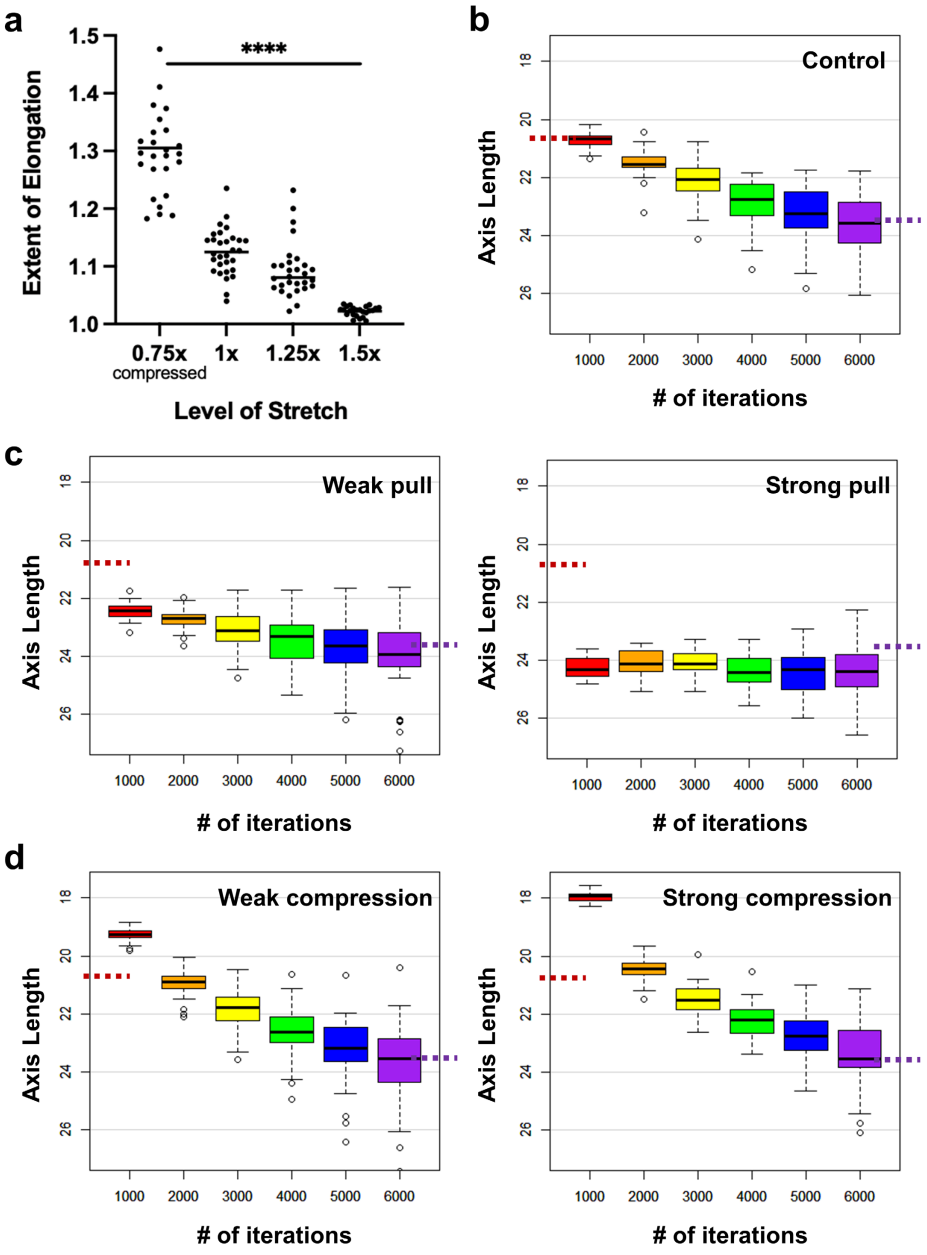

Figure 3. Simulated elongation responses to length perturbations. a. Extent of elongation (defined as the ratio between final simulated axial tissue length over the initial length immediately after the global stretch/compression, with no new cell additions during iterations). n=30 for each group. ****ordinary one-way ANOVA, F=55.98, p=1e-4. **b-d.** Elongation in the 2D model (including new cell additions) with local stretch/compression in the posterior end. n=40 simulations for each test. Dashed red and purple lines mark the average axis lengths in control embryos (panel **b**) at iteration 1000 and 6000, respectively.

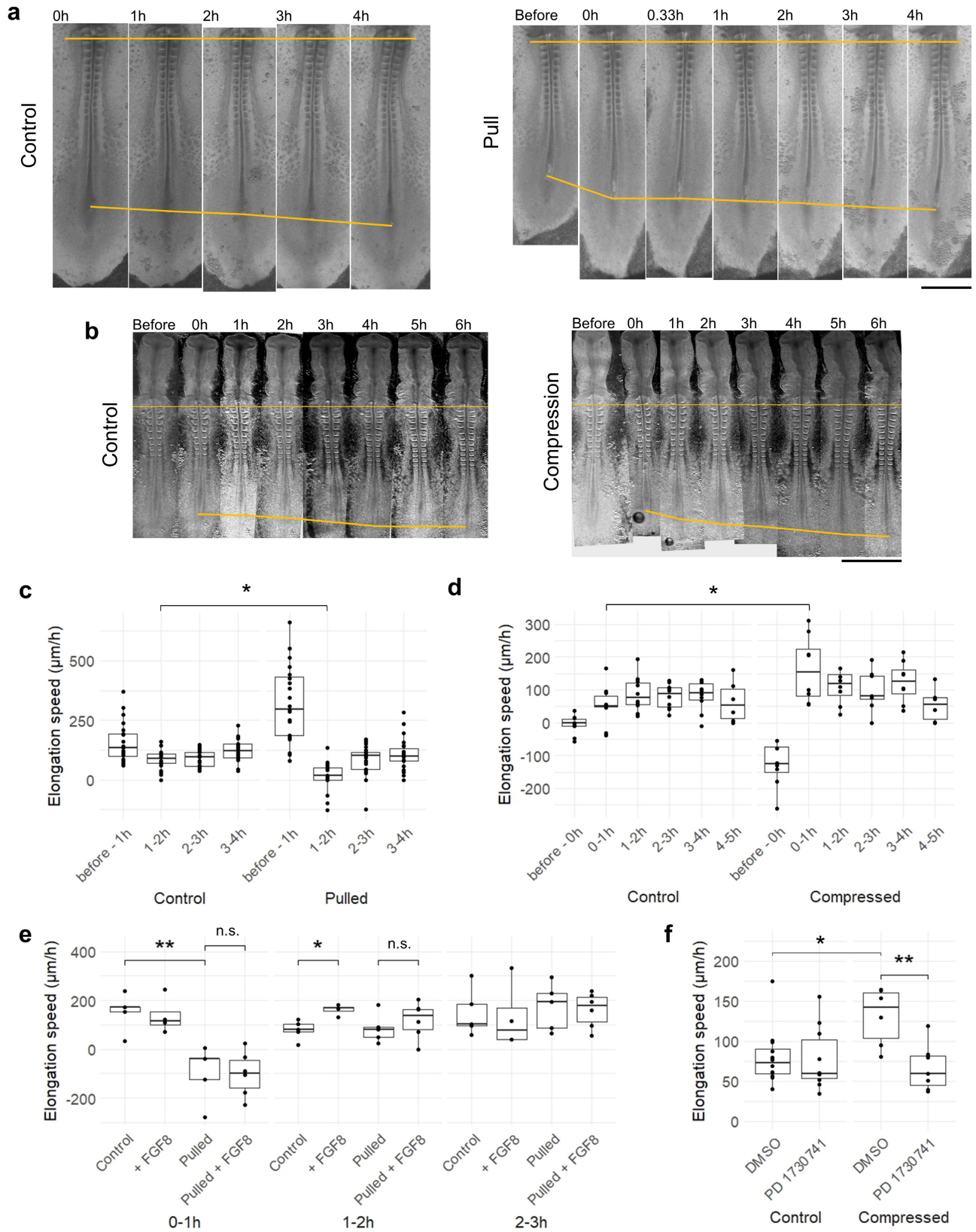

Figure 4. Elongation speed response and robustness to length changes. a-b. Representative embryo changes after pulling (a) and compression (b). The ends of the top

yellow lines mark a somite reference and the ends of the bottom yellow lines mark the end of the axis. Scale bars: 1mm. **c-d.** Elongation speed dynamics following pulling (c, control n=24, pulled n=23, *p= 2e-5, 2 tailed t-tests) and compression (d, control n=10, compressed n=8, for 4-5h n=6 for control and compressed, *p=0.011, 2 tailed t-tests). **e.** Elongation speed dynamics following pulling + FGF8 addition. n=5 for control and pulled, n=4 for +FGF8 and n=6 for pulled + FGF8 (0-1h: **p=3e-3, n.s. p=0.913; 1-2h: *p=7e-3, n.s. p=0.431; 2 tailed t-tests). **f.** Average elongation speed over 4 hours after compression + FGF inhibition. n=12 for control (DMSO), n=10 for FGF inhibitor (PD1730641), n=6 for compressed DMSO and n=7 for PD1730741 (*p=0.011, **p=4e-3, 2 tailed t-tests).

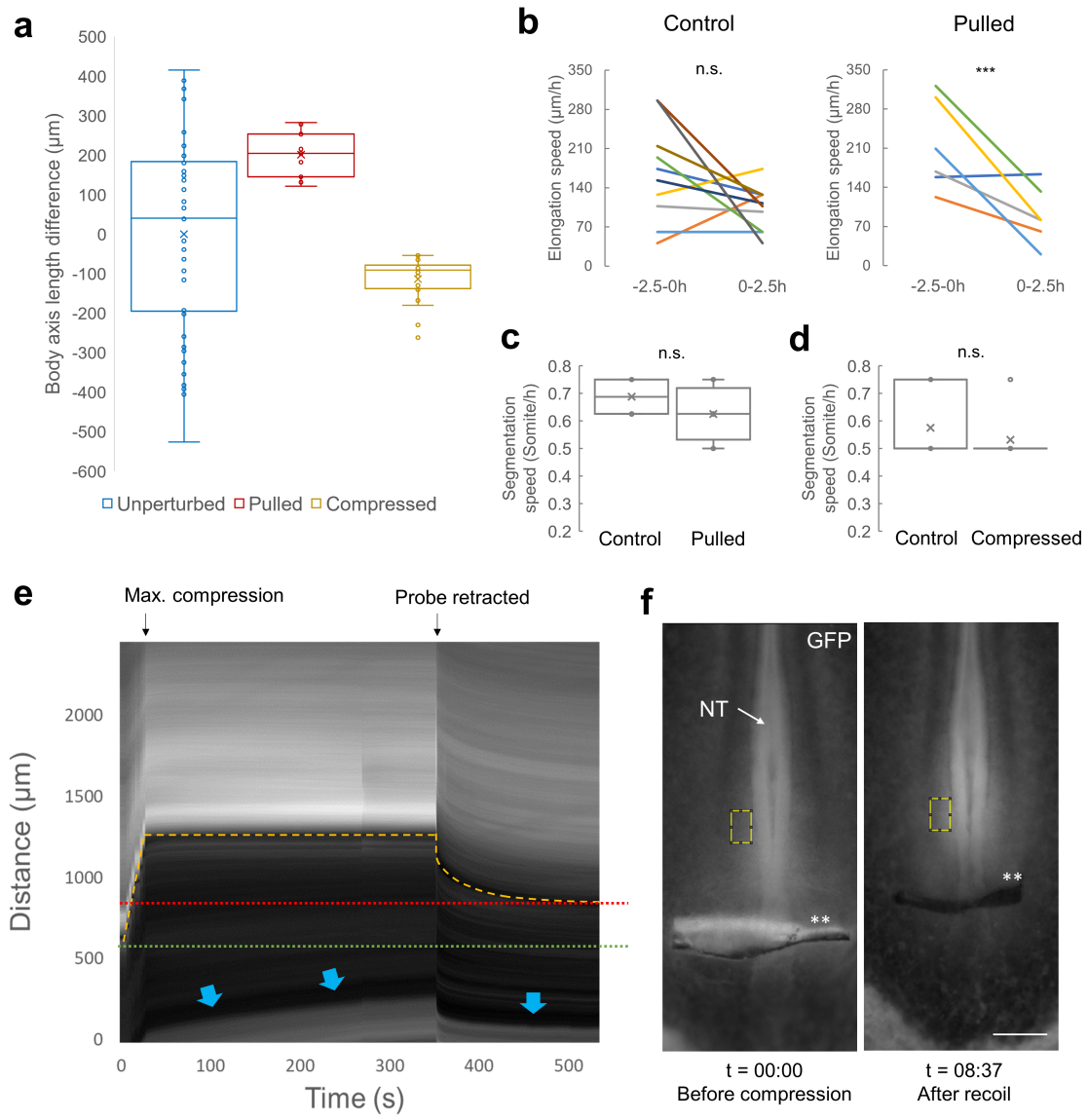

Figure S1. Tissue changes after pulling and compression. a. The variation of body axis lengths in unperturbed embryos (the difference from the population average, n=45) compared to the plastic length changes of pulling and compression experiments (the difference before and after, n=11,20, respectively). Shorter/compressed was defined as negative. **b.** Average elongation speeds in the 2.5h prior to pulling and 2.5h after. n.s., p=0.092, ***p=0.019, paired 2-tailed t-tests. **c.** Segmentation speed. n=8 for controls and n=12 for the pulled (n.s., p=0.118, 2 tailed t-tests). **d.** Segmentation speed. n=10 for controls and n=8 for the compressed (n.s., p=0.405, 2 tailed t-tests). **e.** Kymograph of a compressed embryo, anterior to the top. Dashed yellow line tracks the inserted foil and the slit-wound after its retraction. Red dotted line shows the stable wound location while green dotted line shows the initial position of the foil. Blue arrows highlight the area pellucida and area opaca boundary, which shows a creep behaviour during the holding stage and minimal recoil after probe retraction. **f.** Fluorescence change in compressed pPSM. Mean normalized (to undeformed extraembryonic tissue in the same image) fluorescence

intensities in the tracked yellow boxes are 2.48 pre-compression and 3.74 after recoil, respectively. Asterisks mark the foil/wound location. Scale bar: 300μm.

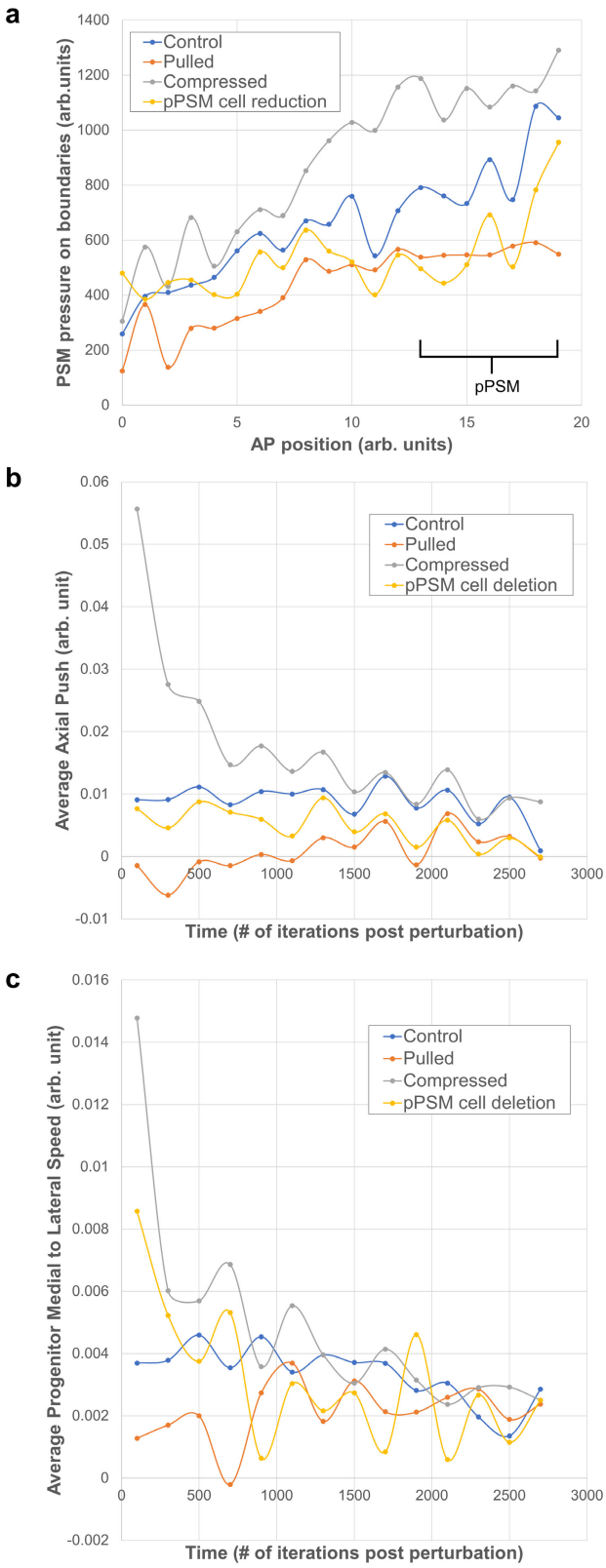

Figure S2. Simulated tissue mechanics and cell dynamics after cell density changes. **a.** Pressure recorded along the AP axis by tallying the collisions and collision strengths of PSM cells with the boundaries of the cell field over time. Results were binned to one average value per unit length (the starting field length is 15 units, pPSM as defined here takes ~5 posterior units up to the posterior-most axial cells). Curves show the average pressures of 10 simulations. Compression and pulling use a parameter of 80 (the same in the strong pull and compression as in Figs.3c-d. pPSM cell deletion causes pressure drop in the pPSM as expected. The pressure increase by compression also affects pPSM more prominently, while pulling causes a more global decrease. **b.** Axial pushing force as measured by the A to P forces on the posterior most axial cells. Results were binned to one average value per 200 iterations after introducing the perturbations. Curves show the average forces of 40 simulations. This force dynamics is directly associated with the elongation speed. A stronger but shorter-lasting increase in the compression is contrasted with a weaker but longer-lasting decrease in the pulling. **c.** PD cells were identified as PSM progenitors that reside on the midline posterior to the axial cells at any given iteration and their medial-lateral speeds were tallied and binned to one average value per 200 iterations after introducing the perturbations. Curves show the average cell flow of 40 simulations.